ACS OMEGA

http://pubs.acs.org/journal/acsodf

Article

Lanthanide-Aromatic Iminodiacetate Frameworks with Helical Tubes: Structure, Properties, and Low-Temperature Heat Capacity

Ming-li Liu,* Quan Shi, Lei-fang Liu, and Wen-bo Li

Cite This: *ACS Omega* 2021, 6, 10475−10485

Read Online

ACCESS | Metrics & More | Article Recommendations | Supporting Information

ABSTRACT: A series of lanthanide coordination polymers $[LnL(H_2O)_2]_n$ [Ln = Pr (**1**), Nd (**2**), Sm (**3**), Eu (**4**), and Gd (**5**), H_3L = *N*-(4-carboxy-benzyl)iminodiacetic acid] was hydrothermally prepared and structurally characterized. All the five compounds have been confirmed as 3D Ln-CPs with one-dimensional helical tunnels composed of four helical chains, although there are different coordination geometries around Ln^{3+}. Enantiomeric helixes in **1**−**3**, and absolute left-handed and right-handed helical chains in **4** and **5**, respectively, lead to different tunnel spaces. Their conformations can also be featured by different space groups and unit cell dimensions. Photoluminescence measurement on **3** and **4** show characteristic emission peaks of Sm^{3+} and Eu^{3+} ions, respectively. The low-temperature heat capacity of **1**−**4** has been investigated in the temperature range of 1.9−300 K. Their heat capacity values are nearly equal below 10 K and display a crossover with the value order $C_{p,m}(2) > C_{p,m}(1) \approx C_{p,m}(4) > C_{p,m}(3)$ above 10 K. The measured heat capacities have been fitted, and the corresponding thermodynamic functions were consequently calculated based on the fitting parameters. The standard molar entropies at 298.15 K have been determined to be (415.71 ± 4.16), (451.32 ± 4.51), (308.53 ± 3.09), and (407.62 ± 4.08) $J \cdot mol^{-1} \cdot K^{-1}$ for **1**, **2**, **3**, and **4**, respectively.

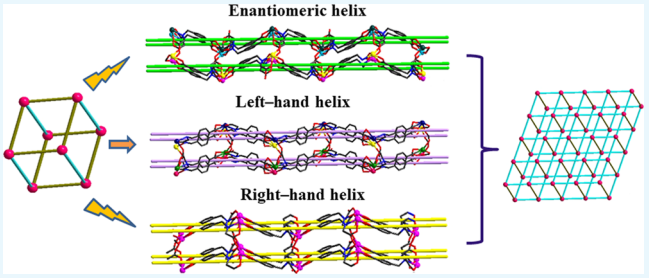

INTRODUCTION

For decades, lanthanide-based coordination polymers (Ln-CPs) as a new type of organic−inorganic hybrid porous materials have attracted a great deal of research interest. Due to their functional properties, versatile applications in different fields have been explored such as gas adsorption and separation,[1−4] magnetic materials,[5−8] molecular recognition[9−14] and detection, dye enrichment and separation,[15,16] and so on. Among them, lanthanide complexes with luminescent properties have been of substantial importance in many applications such as biological imaging, sensing, analysis optical data transfer, and lighting devices.[17−34] Although there is a possibility of the luminescence of Ln^{3+} from intraconfigurational f−f transitions, in the case of irradiation with ultraviolet (UV) radiation, some luminescence in the visible or near-infrared spectral regions can be observed. Such emissions are weak owing to the low absorption of the forbidden f−f transitions. Therefore, some strategies need to be carried out in the process of preparing luminescent Ln^{3+} materials in order to enhance emissive efficiency and decrease the internal nonradiative decay processes. As an important method, appropriate ligands with π-conjugated organic aromatic systems tend to be selected to play a role of "antenna effect". These ligands, such as 1,10-phenanthroline (phen), β-diketones, aromatic carboxylic acid, and so forth, have been proved to be effective in pumping up Ln^{3+} emission and optimize luminescence of complexes.[35−41]

The design and synthesis of new types of Ln-CP-functional materials with intriguing structures are as important as the measurement of their physical properties. Helical structures are among the most explored and best investigated supramolecular architectures. Many single-, double-, meso-, and multihelical complexes generated by self-assembly processes of coordination or supramolecular interactions have been reported.[42−44] What is fascinating about them is not only enchanting motifs but also broad applications in the fields of chiral synthesis, optical devices, sensory functions, and drug delivery.[45−53] However, 3D helical frameworks with helical tunnels (not straight channel formed by helical chains) are not common to our knowledge.

As a useful tool of thermodynamic methods, heat capacity measurement has been utilized to investigate thermal properties of materials at low temperature. From heat capacity, researchers can derive thermodynamic functions of materials, such as entropy, enthalpy, and Gibbs free energy, and further investigate and understand lattice vibrations, metals, superconductivity, electronic and nuclear magnetism, dilute magnetic systems, and structural transitions.[54−58]

As an effective approach, organic compounds with amine appending tend to be used for improving the adsorption

Received: February 26, 2021
Accepted: April 1, 2021
Published: April 12, 2021

Scheme 1. Synthetic Route and Coordination Mode of 1−5

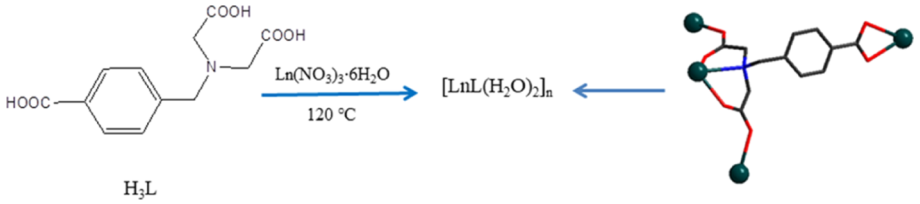

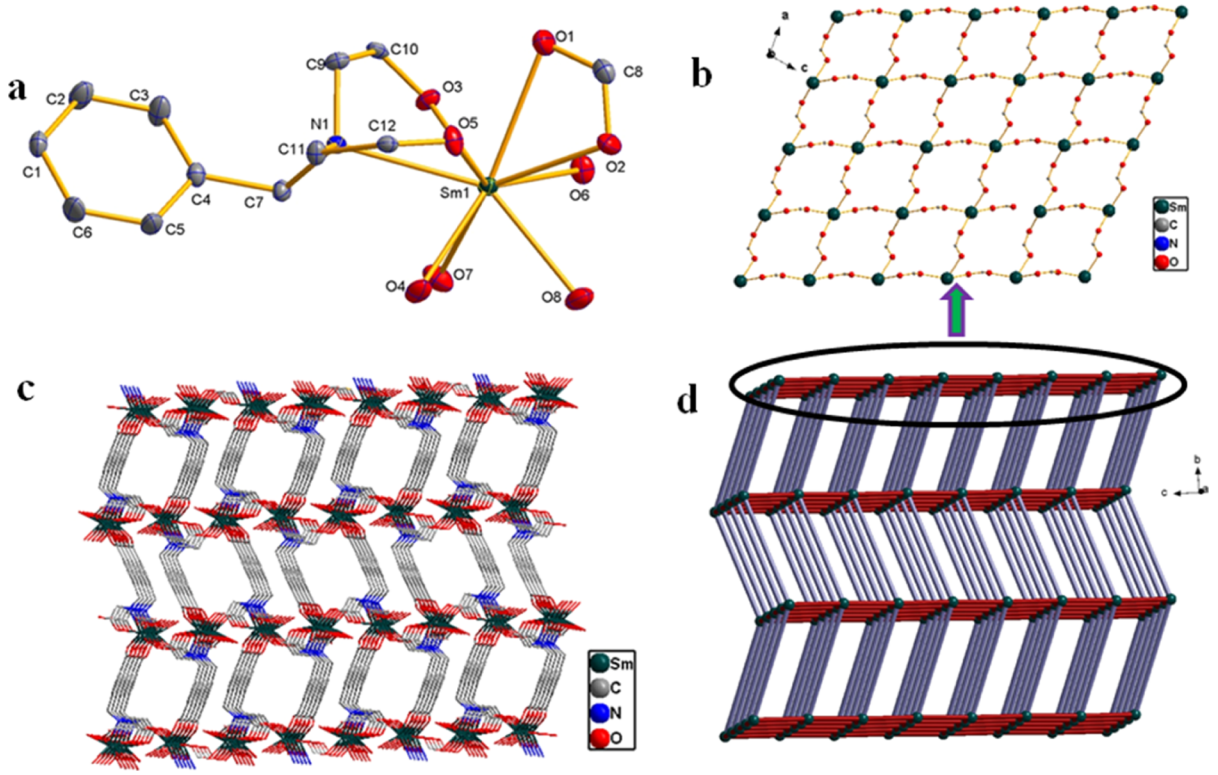

Figure 1. Coordination environment of Sm1 (a), 2D layer structure (b), 3D framework along the *a* direction (c), and 3D topology (d) (−COO bridges and the backbone of L^{3-} are replaced by red and blue lines, respectively) in **3**.

properties of metal−organic frameworks,[59−64] and some flexible ligand containing amino derivatives have been synthesized and used to prepare and stabilize some complexes due to their special coordination characters as tripodal ligands.[65−67] In the present work, as a flexible ligand with aromatic carboxylic acid, *N*-(4-carboxy-benzyl)iminodiacetic acid (Scheme 1), named H_3L, has been used to synthesize some Ln-Cps. A series of coordination polymers with the formula $[LnL(H_2O)_2]_n$ have been synthesized (Scheme 1) and structurally characterized. Their fluorescent properties, magnetic properties, and thermal stability have also been studied. Furthermore, the heat capacities of **1−4** have been measured over the temperature range (from 1.9 to 300 K) using a PPMS calorimeter. The experimental data have been fitted to a series of theoretical functions, and the corresponding thermodynamic functions have been calculated based on these fits.

RESULTS AND DISCUSSION

Crystal Structure Descriptions. *Structure of 1−3.* **1**, **2**, and **3** are isomorphous and crystallized in the monoclinic space $P2_{(1)}/n$. Therefore, the molecular structure of **3** is described in detail. As shown in Figure 1a, the asymmetric unit $[SmL(H_2O)_2]$ is composed of one Sm^{3+} ion, one L^{3-} ligand, and two H_2O molecules. The Sm^{3+} ion is surrounded by an environment of NO_8. Six oxygen atoms are supported by three carboxylate groups of different L^{3-} ligands. The rest two O atoms come from coordinated H_2O molecules. All the Sm−O bond lengths fall in the range of 2.42−2.67 Å. The N atom is provided by the L^{3-} ligand with a distance of 2.727(6) Å to Sm^{3+}. All Sm−N/O distances are in agreement with literature data.[68,69] As illustrated in Figure 2, the coordinated NO_8 around Sm^{3+} forms a distorted single-capped antitetraprism. In the process of binding with Sm^{3+}, three carboxylic groups of the deprotonated ligand L^{3-} show two kinds of coordination modes: *syn-anti* 211 (acetic group) and common 111 (carboxylic group).[70] Neighboring Sm^{3+} ions are linked by two acetic groups *via syn-anti* 211 in the *ac* plane, resulting in a perfect 2D planar with a 4·4 topology and Sm...Sm distances of 6.18 and 6.05 Å. Furthermore, the 4·4 2D networks (Figure 1b) extend to become a twisted 3D framework by *η*-L^{3-} (Figure 1c,d). The Sm...Sm distance bridged by ligands is 12.03 Å. It is worth noting that the 3D framework constructed by L^{3-} and Ln^{3+} is different from the known one-dimensional (1D) structures,[71] in which partially deprotonated H_3L coordinated with Ln^{3+} and formed 1D linear arrangement. In our research, three complexes exhibit a Ln-CP framework with

https://doi.org/10.1021/acsomega.1c01052
ACS Omega 2021, 6, 10475−10485

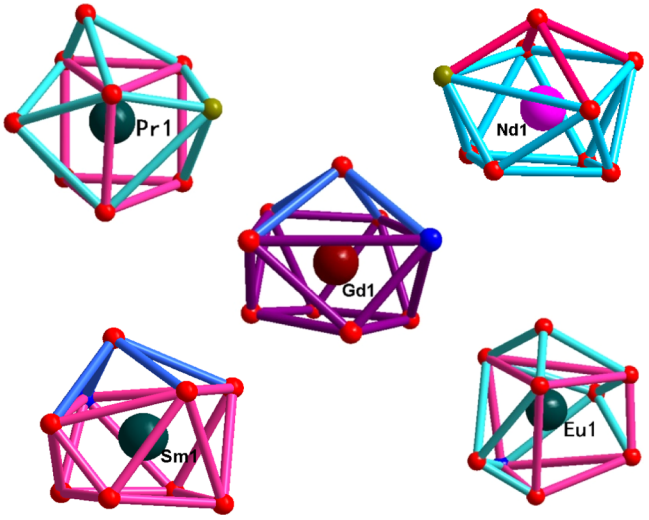

Figure 2. Coordination geometries around Ln^{3+} in **1**−**5**.

some tunnel vacancies, whose sizes (regardless of the van der Waals radius) have been listed in Table S1.

To our surprise, an interesting 1D tunnel can be observed along the *b* direction, as illustrated in Figure 3a,b,f. They are not linear or *Z*-shaped tunnels but helical tunnels. Each tunnel was constructed by four helical chains, as illustrated in Figure 3f, in which two are left-handed helical chains (Figure 3c) and the other two are right-handed helical chains. Each couple of helical chains was bridged by −COO groups and formed a spiral belt (Figure 3d). Further carboxylic linking between two spiral belts eventually led to a helical tunnel with enantiomeric conformation (Figure 3e) in **3**. For this, the tunnels along the *b* direction become inhomogeneous. As for **1**, the structure and framework are similar to those of **3**, except for the three-cap triangle prism geometry (Figure 2) around Pr^{3+} ions. All Pr−O/N lengths in the range of 2.449−2.530 Å together with longer Pr1-O1$^{\#1}$ [2.693(4) Å] and Pr1-N1 [2.745(5) Å] are normal compared with some reported Pr^{3+} compounds.[72] Other relevant data about **1**−**3** are listed in Tables S1 and S2.

Structure of ***4****.* **4** also crystallized in a monoclinic system but has a $P2_{(1)}$ space group. The structure of the asymmetric unit $[EuL(H_2O)_2]$ is similar to that of **1** except for a different three-cap triangle prism geometry around Eu^{3+}. The Eu−O distances are in the range of 2.39−2.486 Å along with two longer bonds Eu1-O2$^{\#1}$ [2.630(15) Å] and Eu1-N1 [2.73(2) Å], which constructed a distorted triangle prism with edge lengths of 2.213, 3.477, and 3.501 Å. Due to flexible single bond of $-CH_2-$N, the phenyl ring can rotate to some extent, which may lead to different molecule conformations. Such an interesting phenomenon just exists in **4**. The framework (Figure 4a) is inconsistent with **3** (Figure 1c), although its topology structure (Figure 4b), also with a1D helical tunnel, is similar to that of **3**. Further study revealed that all the four chains in the 1D tunnel in the *b* direction are left-handed helices (Figure 4c). Two helical chains were bridged by −COO groups, leading to a left-handed helical belt like that in **3**. Then, still linked by carboxylic bridges, two left helical belts formed a helical tunnel.

Structure of ***5****.* **5** crystallized in monoclinic system with a $P2_{(1)}$ space group. The asymmetric fragment $[GdL(H_2O)_2]$ is similar to that of **3** with a single-capped antitetraprism environment around Gd^{3+}. Gd−O/N distances are 2.335−2.467 Å besides long Gd1-O2 [2.74(3) Å] and Gd1-N1 [2.740(14) Å], all of which lie in the normal Gd−O/N bond length range.[72] Obviously, it is a distorted antitetraprism. The spatial structure of **5** is similar to that of **4**, as seen in Figure 4d,e. While, the difference can be found out whether its 1D chain, belt, or tunnel form is a right-handed helix (Figure 4f).

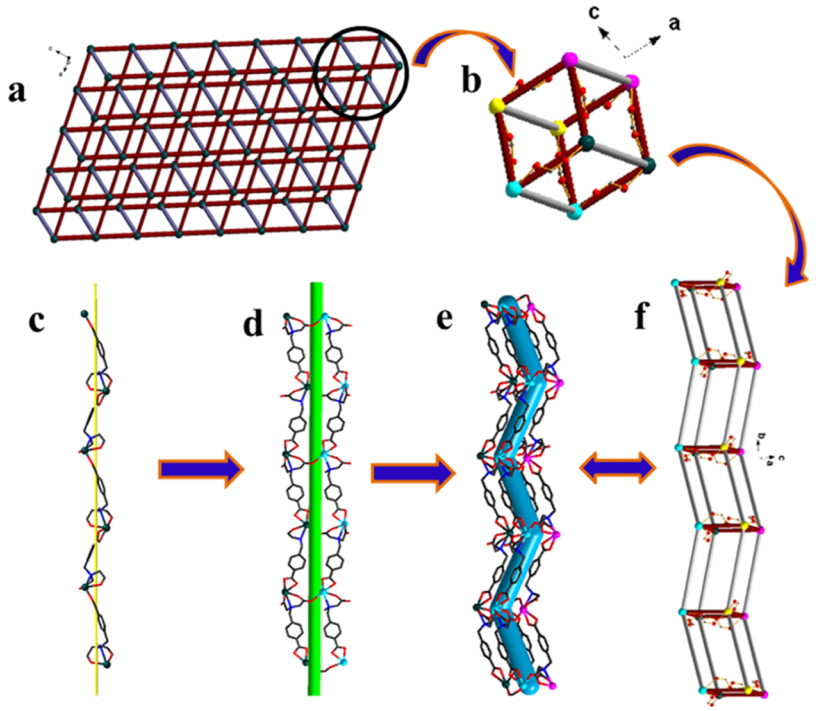

Figure 3. (a) 3D topological framework of **3**. (b) and (f) 1D helical tunnel along the *b* direction. (c) 1D left-handed helical chain formed by Sm^{3+} and backbones of L^{3-}. (d) 1D helical belt formed by the double left-handed helical chain. (e) 1D helical tunnel formed by two enantiomers.

https://doi.org/10.1021/acsomega.1c01052
ACS Omega 2021, 6, 10475−10485

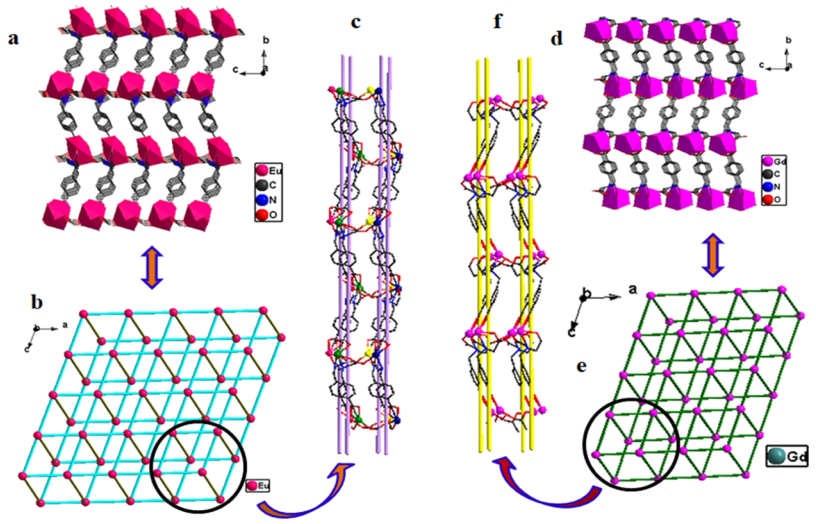

Figure 4. 3D framework (a) and (d), topology structure (b) and (e), and 1D helical tunnel (c) and (f) for **4** and **5**, respectively.

The relevant intermetallic distance and angles can be found in Table S1.

Powder X-ray Diffraction Patterns and Thermogravimetric Analysis Data. To confirm the phase purity, powder X-ray diffraction (XRD) on crystal samples **1**−**5** was carried out in the 2θ range of 5−60° at room temperature (Figure S1). The experimental XRD patterns were compared to their corresponding simulated patterns calculated based on single crystal diffraction data. The result indicates that all of the samples are in the pure phase.

The thermogravimetric analysis (TGA) data in the temperature range of 30−700 °C for **3** and **5** and 20−800 °C for **1**, **2**, and **4** are shown in Figures S2 and S3. Upon heating, samples **1** and **4** lost their weight at approximately 100 °C and then showed three and two steps of weight loss above this temperature, respectively. For **1**, two-step weight loss in the ranges of 100−213 and 213−353 °C occurred with values of 4.73 and 8.4%, respectively, consistent with the weight of one coordinated H_2O (calcd 4.27%) and one −COO (10.45%). While the loss of H_2O and −COO in **4** are consecutive with a sum value of 13.6% (calcd 14.34%) in the range of 100−320 °C. **1** and **4** exhibited quick decomposition above 378 and 335 °C, with the remainder weight 54 and 50.84% at 700 °C, respectively. **2**, **3**, and **5** also lost weight from 100 °C and showed obvious stages in the range of 285−375, 262−362, and 272−371 °C, respectively. The losses were 9, 9.4, and 8.9% in the lower-temperature region, nearly equal to the weight of two H_2O molecules (calcd 8.17, 8.06, and 7.94% for **2**, **3**, and **5**, respectively). **2**, **3**, and **5** decomposed at higher temperatures.

Photoluminescence Properties. The solid-state photoluminescence properties of **1**−**5** were measured at room temperature. Under the excitation at 275 nm, **1** and **2** show no lanthanide-based emission peaks, indicating the mismatch of the energy levels of L^{3-} so that the energy could not be effectively transmitted. When excited at 265 nm, **3** and **4** gave rise to lanthanide-based emission, as shown in Figures 5 and 6, showing efficient ligand-sensitized f−f emission. The characteristic Sm^{3+} emission peaks are observed at 560, 595, and 642 nm, which are attributed to $^4G_{5/2} \rightarrow {}^6H_{5/2}$, $^4G_{5/2} \rightarrow {}^6H_{7/2}$, and $^4G_{5/2} \rightarrow {}^6H_{9/2}$, respectively. The expected Eu^{3+} characteristic emission peaks for **4** appear at 579, 591, 617, 651, and 697 nm, which belong to the transitions $^5D_0 \rightarrow {}^7F_J$ (J = 0−4) (Figure 6).

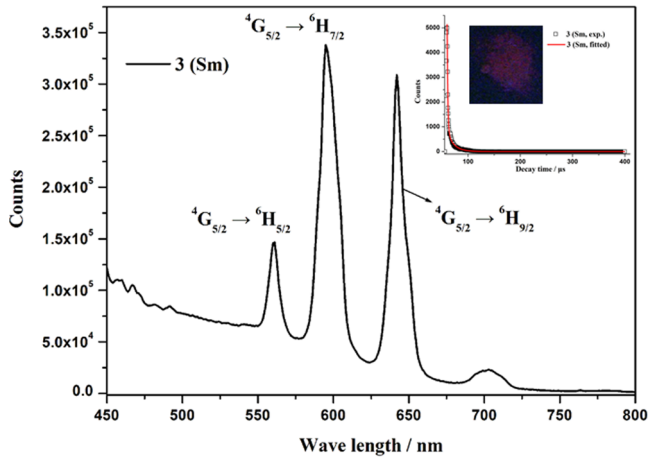

Figure 5. Solid-state emission spectra, emission decay patterns, and emission photo under UV light (insets) of **3**.

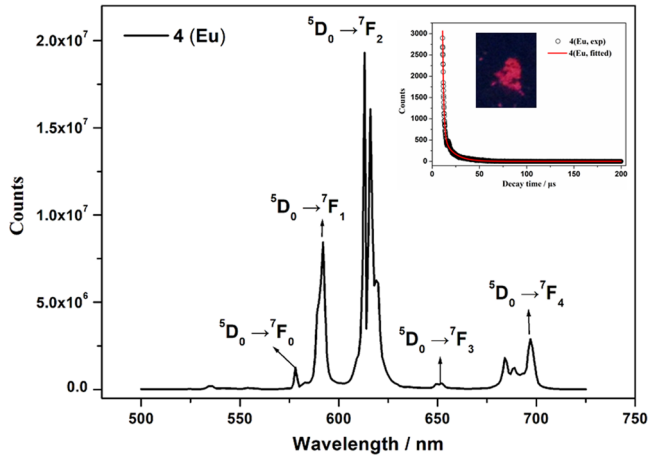

Figure 6. Solid-state emission spectra, emission decay patterns, and emission photo under UV light (insets) of **4**.

According to the transition rules of Eu^{3+} ions, when Eu^{3+} ions occupy the inversion centers, the magnetic dipole transitions ($^5D_0 \rightarrow {}^7F_1$) are dominant, emitting orange light; when Eu^{3+}ions dwell in the noninversion sites, the electric dipole transitions

https://doi.org/10.1021/acsomega.1c01052
ACS Omega 2021, 6, 10475−10485

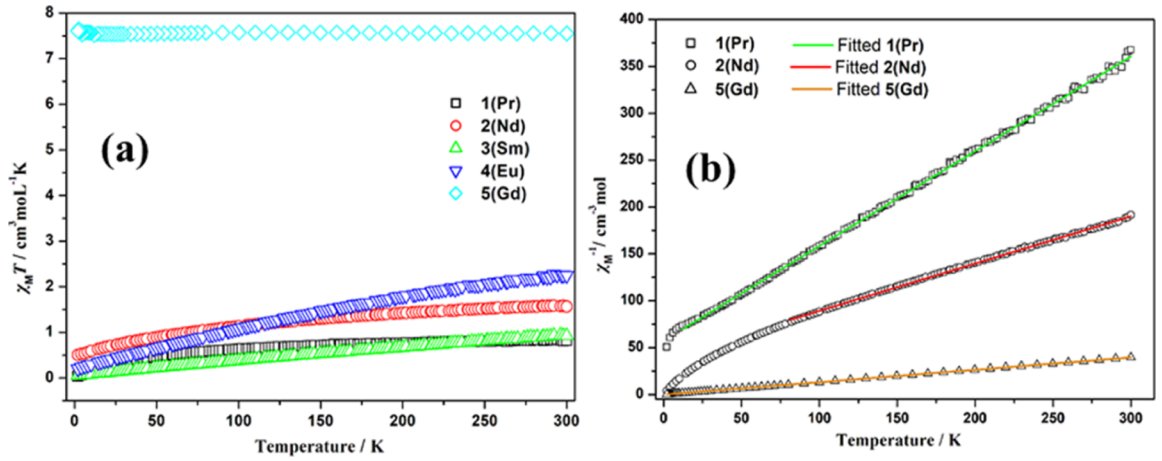

Figure 7. (a) Plot of $\chi_M T$ *versus* T for **1**−**5**. (b) Plot of χ_M^{-1} *versus* T for **1**, **2**, and **5**.

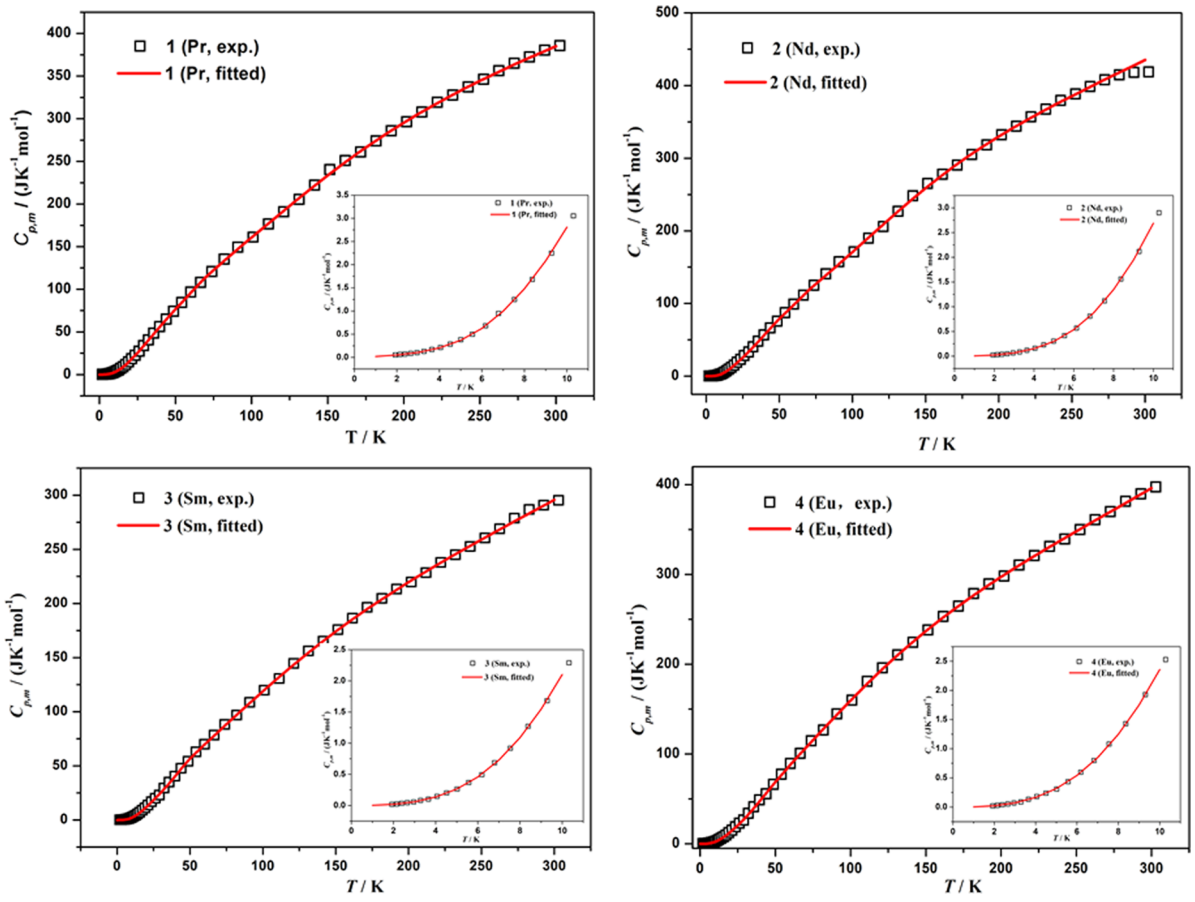

Figure 8. Plot of the experimental and fitted heat capacities of **1**−**4** as a function of temperature ranging from 2 to 300 K. The inset shows the data below 10 K.

($^5D_0 \rightarrow {}^7F_2$) are regnant, emitting red light.[73−75] The high ratio of intensity ($^5D_0 \rightarrow {}^7F_2/{}^5D_0 \rightarrow {}^7F_1$) suggests that the Eu^{3+} ions occupy the low-symmetry coordination sites with no inversion centers, which is consistent with the result of the XRD structural analysis. When exposed under an UV lamp, **3** and **4** emit dark red and bright red light [Figures 5 and 6 (insets)], respectively. Time-resolved luminescence measurement on **3** and **4** has been carried out. The result showed lifetimes of 2 and 8 μs (calculated by the formula $[\tau] = (A_1\tau_1 + A_2\tau_2)$) obtained *via* double-exponential fitting [Figures 5 and 6 (inserted)].

Magnetic Properties. The d.c. molar magnetic susceptibilities of **1**−**5** were measured on polycrystalline samples in the temperature range 2−300 K under an applied magnetic field of 1 kOe. The experimental results are shown in Figure 7 in the form of $\chi_M T$ products. At room temperature, the $\chi_M T$ products of **1**−**5** have values of 0.845, 1.589, 0.918, 2.254, and 7.561 cm^3 K mol^{-1}, respectively. They are in agreement with the expected theoretical values for a single Pr^{3+} (1.6 cm^3 K mol^{-1}, $^3H_4$, g = 4/5), Nd^{3+} (1.64 cm^3 K mol^{-1}, $^4I_{9/2}$, g = 8/11), and Gd^{3+} (7.88 cm^3 K mol^{-1}, $^8S_{7/2}$, g = 2). Free Sm^{3+} ions have the $^6H_{5/2}$ ground term, which is split into six states by spin−orbit coupling at room

https://doi.org/10.1021/acsomega.1c01052
ACS Omega 2021, 6, 10475−10485

Table 1. Summary of Heat Capacity Fitting Parameters of 1−4

parameters	**1** (Pr)	**2** (Nd)	**3** (Sm)	**4** (Eu)
		low *T* fits		
$\gamma/(J\cdot mol^{-1}\cdot K^{-2})$	0.019504	0.003471	0.001827	0.001229
$B_3/(J\cdot mol^{-1}\cdot K^{-4})$	0.001618	0.001928	0.001981	0.002551
$B_5/(J\cdot mol^{-1}\cdot K^{-6})$	2.65×10^{-5}	1.57×10^{-5}	3.41×10^{-6}	-2.1×10^{-6}
$B_7/(J\cdot mol^{-1}\cdot K^{-8})$	-1.7×10^{-7}	-8.7×10^{-8}	-2.5×10^{-8}	
%RMS	2.434516	1.687415	2.879716	2.736678
range/K	6.94	9.26	7.96	10
		mid. *T* fits		
A_0	0.163477	−0.82247	−1.08956	−0.96548
A_1	−0.01039	0.602612	0.66634	0.536592
A_2	−0.01855	−0.16616	−0.16089	−0.12081
A_3	0.007377	0.023535	0.021321	0.016657
A_4	−0.00035	−0.00124	−0.00116	−0.00088
A_5	8.49×10^{-6}	3.52×10^{-5}	3.41×10^{-5}	2.52×10^{-5}
A_6	-1.2×10^{-7}	-5.6×10^{-7}	-5.6×10^{-7}	-4.1×10^{-7}
A_7	9.13×10^{-10}	4.65×10^{-9}	4.78×10^{-9}	3.45×10^{-9}
A_8	-3×10^{-12}	-1.6×10^{-11}	-1.7×10^{-11}	-1.2×10^{-11}
%RMS	1.1062	0.729392	1.525526	1.343216
range/K	from 6.94 to 67	from 9.26 to 67.9	from 7.96 to 57.1	from 10 to 55.05
		high *T* fits		
m	6.89743	9.949089	3.013084	5.856802
θ_D/K	230.0283	208.8382	206.135	216.1289
n	8.761887	14.2764	3.889093	7.563872
θ_E/K	626.667	566.2246	496.7288	492.2791
$A_1/(J\cdot K^{-2}\cdot mol^{-1})$	0.049089	−0.93601	0.368435	−0.03802
$A_2/(J\cdot K^{-3}\cdot mol^{-1})$	0.000548	0.002298	0.000381	0.001261
%RMS	0.67775	0.767591	0.661001	0.553843
range/K	above 67	above 67.9	above 57.1	above 55.05

temperature; however, the ground state $^6H_{5/2}$ is not well separated from the excited ones (around 700 cm^{-1} from the ground state to the first excited state), so both the crystal field effect and possible thermal population of the high states should be evaluated for the Sm^{3+} complex. The $\chi_M T$ value at 300 K is larger than the expected spin-only value for isolated Sm^{3+} (0.088 cm^3 K mol^{-1}, $^6H_{5/2}$, g = 2/7). The value of $\chi_M T$ decreases rapidly to 0.0554 cm^3 K mol^{-1} at 2 K and is nearly linear over the whole temperature range, which is similar to that of other reported Sm^{3+} complexes.[76] As for the case of **4**, because the low-lying $^7F_1$ first excited state is partly populated at room temperature, a finite magnetic moment appears at room temperature, although the $^7F_0$ ground state of Eu^{III} possesses no magnetic moment, and thus, Eu^{3+} should be diamagnetic at low temperature. Finally, the $\chi_M T$ product of **4** decreases continuously upon cooling and reaches 0.203 cm^3 K mol^{-1} at 2 K, reflecting the thermal depopulation of the $^7F_1$ first excited state upon cooling, likely indicating mixing of the $^7F_0$ ground state with excited states possessing a magnetic moment.[77] The $\chi_M T$ products of **1** and **2** remain nearly constant down to approximately 100 K, wherefrom it begins to decrease upon further cooling to reach 0.037 and 0.505 cm^3 K mol^{-1} at 2 K, respectively. This behavior could be an indication of weak antiferromagnetic exchange interactions. Such results could also be predicted from the classical single *syn-anti*-OCO bridge within the 2D layer, which is the most likely pathway for the antiferromagnetic exchange.[78,79] The $\chi_M T$ product of **5** is nearly unchanged up to 10 K. Then, the plot shows an increasing trend in $\chi_M T$ up to 7.6 cm^3 K mol^{-1} at 2 K (Figure 7), which is possibly due to weak ferromagnetic interactions between adjacent Gd^{3+} centers in **5**. Compared with some Gd^{3+} compounds,[80] the deviation of $\chi_M T$ is not evident. The χ_M^{-1} *versus* T over different temperature ranges for **1**, **2**, and **5** were fitted to the Curie−Weiss law $\chi_M = C/(T - \theta)$ (Figure 7b). **5** obeys the Curie−Weiss law over the entire temperature range with the Curie constant C = 7.56 cm^3 K mol^{-1} and the Weiss constant θ = −0.002, indicating the faint interactions between neighboring Gd^{3+}. Since χ_M^{-1} *vs* T deviated from the Curie−Weiss law in low-temperature zone, the fitting of magnetic data was carried out over 10−298 K for **1** and 80−298 K for **2**, respectively, with the Curie constant C and the Weiss parameter θ of 0.99 cm^3 K mol^{-1} and −56.89 K for **1** and 1.98 cm^3 K mol^{-1} and −77.2 K for **2**, respectively.

Low-Temperature Heat Capacity. The heat capacity of crystalline samples **1**−**4** measured by the PPMS are given in Tables S3−S6 and plotted *vs* T in Figure 8. With the temperature increasing, it can be observed that the heat capacity increases smoothly and no thermal anomalies are found in the total experimental region. In fact, there is an interesting phenomenon seen from the graphs in Figure S4. The experimental heat capacity tendency below 10 K is hardly distinguished for them. With heating, larger and larger $C_{p,m}$ differences were observed among them. In general, the heat capacity data order is $C_{p,m}(\mathbf{2}) > C_{p,m}(\mathbf{1}) \approx C_{p,m}(\mathbf{4}) > C_{p,m}(\mathbf{3})$ in the range of 10−300K. Outwardly, the analogous coordination geometry around Ln^{3+} in **2** and **3** should lead to approximate heat capacity values. While, the case is not that. The large difference in $C_{p,m}$ values between them may be effected by lanthanide contraction. Although effected by lanthanide contraction, the $C_{p,m}$ difference between **1** and **4** is small, which may be due to the distortion of geometric configuration around Ln^{3+} ions.

Modeling heat capacity data with theoretical functions at low temperature can provide valuable information about magnetic,

https://doi.org/10.1021/acsomega.1c01052
ACS Omega 2021, 6, 10475−10485

electronic, and vibrational properties of a sample.[81,82] All the total heat capacities can be viewed as a sum of energetic contributions from the various physical properties of a material. The lattice contribution is relatively small below around 10 K, where the other properties can be extracted by fitting the experimental heat capacity to theoretical functions. The heat capacity data below around 10 K were fitted to the following equation

$$C_{p,m} = \gamma T + \sum_{n=3,5,7\ldots} B_n T^n \quad (1)$$

$$C_{p,m} = A_0 T^0 + A_1 T^1 + A_2 T^2 + A_3 T^3 + A_4 T^4 + A_5 T^5 + A_6 T^6 + A_7 T^7 + A_8 T^8 \quad (2)$$

$$C_{p,m} = n_D \times D(\theta_D/T) + n_E \times E(\theta_E/T) + A_1 \times T^1 + A_2 \times T^2 \quad (3)$$

where the linear fashion with γT represents the electronic contribution of conductors and defect or oxygen vacancies for insulators; the odd powers in temperature represent the lattice.[83] For compounds **1**−**3**, the values of n are 3, 5, and 7, respectively. However, n = 7 does not necessarily fit to the data of **4**.

The data in the middle temperature range for **1**−**4** are fitted to an arbitrary polynomial of eq 2. For the high temperature, the data are fitted to eq 3,[83,84] a combination of Debye and Einstein functions, where $D(\theta_D)$ and $E(\theta_E)$ are Debye and Einstein functions, respectively, and T and T^2 terms constitute an approximation of $(C_{p,m} - C_{V,m})$. All the fitting parameters are listed in Table 1, and the fitted heat capacity is shown in Figure 8.

As seen in Figure 8, the fits match the experimental heat capacity well. Low-temperature fitting suggests that although the γT contributions for **1**−**4** are different, the C_p values are comparable since the difference can be weakened by the contribution from their lattice vibration modes. With the temperature increasing, the electronic contribution becomes insignificant, while the contribution of lattice vibration to C_p is dominant.

Based on these fitting results, the corresponding thermodynamic functions have been calculated, and the calculated values of ΔS_m and ΔH_m have been listed in Tables S3−S6. The standard molar entropy and standard molar enthalpy at T = 298.15 K for **1**−**4** are (415.71 ± 4.16) J·mol^{-1}·K^{-1} and (64.29 ± 0.64) kJ·mol^{-1}, (451.32 ± 4.51) J·mol^{-1}·K^{-1} and (71.03 ± 0.71) kJ·mol^{-1}, (308.53 ± 3.09) J·mol^{-1}·K^{-1} and (48.05 ± 0.48) kJ·mol^{-1}, and (407.62 ± 4.08) J·mol^{-1}·K^{-1} and (64.45 ± 0.64) kJ·mol^{-1}, respectively. The four complexes display an $\Delta_0 298.15 S_m$ order: (**2**) > (**1**) ≈ (**4**) > (**3**), which is consistent with their $C_{p,m}$ order.

CONCLUSIONS

A series of lanthanide coordination polymers were isolated as single crystals under hydrothermal conditions. All of them formed 2D planar 4·4 layers *via* −COO bridges and extended to be 3D frameworks through L^{3-} bridges. Although there are helical tunnels in all of the five compounds, the framework conformations are different due to the flexible L^{3-} and various coordination geometries around metal centers. The helical tunnels in **1**−**3** are constructed by two pairs of enantiomeric helical chains, which gave rise to large intervals and small space. While, four pure left-handed and right-handed helical chains in **4** and **5**, respectively, construct a uniform tunnel space. The changes in the tunnel space may be possible in transport of some ions or small molecules. Further studies need to be carried out to reveal this property. Characteristic Sm^{3+} and Eu^{3+} emitting can be seen from emission spectra. **3** emits dark-red luminescence and **4** emits bright-red luminescence under UV light. Unfortunately, the luminescent lifetime is short owing to the coordination of H_2O to metal ions and absence of a long conjugate system. Single *syn-anti*-OCO bridges between Ln^{3+} ions lead to weak magnetic interactions. The heat capacities of **1**−**4** have been studied using a Quantum Design PPMS calorimeter over the temperature range from (1.9 to 300) K, and the standard thermodynamic functions have been derived based on the fitted experimental data. The standard molar entropies at T = 298.15 K have been calculated to be (415.71 ± 4.16)$^{---}$, (451.32 ± 4.51)$^{---}$, (308.53 ± 3.09)$^{---}$, and (407.62 ± 4.08) J·mol^{-1}·K^{-1}, respectively.

EXPERIMENTAL SECTION

Materials and Methods. All chemicals and solvents were of the analytical grade and were obtained from commercial sources and used without further purification. The starting ligand *N*-(4-carboxy- benzyl)imino diacetic acid (H_3L) was synthesized according to the methods already reported.[85,86]

Elemental analyses were carried out on an Elementer Vario Micro Cube analyzer. The FT-IR spectra were measured on a Thermo Niclet IR00 FT-IR spectrometer using KBr pellets (range of 4000−500 cm^{-1}). A SIMADZU DTG-60 thermo analyzer was used to perform the TGA under nitrogen at a heating rate of 5 °C min^{-1} from room temperature to 700 °C. Powder XRD (PXRD) data under the 2θ range 5−60° were recorded using Cu Kα radiation (κ = 0.1542 nm) on a Bruker D8A A25 X-ray diffractometer, with the X-ray tube operated at 40 kV and 40 mA at room temperature. Luminescence properties were recorded on an FLS980 spectrophotometer with a Xe lamp as the light source at room temperature.

Preparation. *[LnL(H$_2$O)$_2$]$_n$*. A mixture of Ln(NO$_3$)$_3$·6H$_2$O (0.20 mmol) (Ln = Pr **1**, Nd **2**, Sm **3**, Eu **4** and Gd **5**) and H_3L (0.20 mmol) in 8 mL of distilled water was sealed into a 25 mL Teflon-lined stainless steel reactor and heated at 120 °C for 3 days (Scheme 1). Then, the mixture was cooled to room temperature at an approximate rate of 5 °C h^{-1}. Suitable single crystals for XRD were obtained by filtration.

*[PrL(H$_2$O)$_2$]$_n$ (**1**)*. Yield: 32% (based on Pr). Anal. Calcd for $C_{12}H_{14}NO_8Pr$ (%): C, 32.64; H, 3.17; N, 3.17. Found (%): C, 32.88; H, 2.97; N, 3.13. IR (KBr, cm^{-1}): 3423 (vs), 2937 (w), 1582 (vs), 1524 (s), 1397 (vs), 1324 (s), 1252 (s), 1092 (m), 1009 (w), 975, 931 (m), 848 (m), 785, 703 (m), 538 (w).

*[NdL(H$_2$O)$_2$]$_n$ (**2**)*. Yield: 36% (based on Nd). Anal. Calcd for $C_{12}H_{10}NO_8Nd$ (%): C, 32.40; H, 3.15; N, 3.15. Found (%): C, 32.72; H, 2.84; N, 3.40. IR (KBr, cm^{-1}): 3384 (vs), 2939 (w), 1594, 1575 (vs), 1522 (s), 1400 (vs), 1332 (s), 1251 (m), 1085 (s), 1008, 972, 932 (m), 855, 815, 785 (m), 716 (m), 540 (w).

*[SmL(H$_2$O)$_2$]$_n$ (**3**)*. Yield: 34% (based on Sm). Anal. Calcd for $C_{12}H_{14}NO_8Sm$ (%): C, 31.96; H, 3.11; N 3.11. Found: C, 31.46; H, 3.44; N, 3.08. IR (KBr, cm^{-1}): 3426 (vs), 2934 (w), 1586 (vs), 1530 (s), 1404 (vs), 1327 (s), 1249 (m), 1095 (s), 1018, 983, 933 (m), 863, 814, 779 (m), 547 (w).

*[EuL(H$_2$O)$_2$]$_n$ (**4**)*. Yield: 38% (based on Eu). Anal. Calcd for $C_{12}H_{14}NO_8Eu$ (%): C, 31.84; H, 3.10; N, 3.10. Found (%): C, 32.07; H, 3.23; N, 3.17. IR (KBr, cm^{-1}): 3433 (vs), 2933 (w),1577 (vs), 1525 (s), 1405 (vs), 1321 (s), 1243 (m), 1092 (s), 1009, 972, 931 (m), 852, 816, 779 (m), 534 (w).

https://doi.org/10.1021/acsomega.1c01052
ACS Omega 2021, 6, 10475−10485

$[GdL(H_2O)_2]_n$ (**5**). Yield: 29% (based on Gd). Anal. Calcd for $C_{12}H_{14}NO_8Gd$ (%): C, 31.48; H, 3.06; N, 3.06. Found (%): C, 31.41; H, 2.75; N, 3.16. IR (KBr, cm^{-1}): 3422 (vs), 2940 (w), 1590 (vs), 1519 (vs), 1416 (vs), 1320 (s), 1243 (m), 1103 (m), 1023, 979, 936 (w), 863, 819, 776 (m), 543 (w).

X-Ray Crystallography. Single-crystal XRD data of the complexes **1**−**5** were collected on a Bruker SMART APEXII CCD diffractometer equipped with graphite monochromated Mo Kα radiation (λ = 0.71073 Å). The SADABS programs were used to apply the empirical absorption correction. Direct methods and full-matrix least-squares methods on F^2 were performed to solve and refine the structure using the program SHEXL-2014.[87−89] All nonhydrogen atoms were refined anisotropically. The hydrogen atoms whose positions and thermal parameters were fixed during the structure refinement were located by geometrical calculations. The crystallographic data and details (Table S7) and selected bond lengths and angles (Table S2) are summarized in the Supporting Information.

■ ASSOCIATED CONTENT

Supporting Information

The Supporting Information is available free of charge at https://pubs.acs.org/doi/10.1021/acsomega.1c01052.

Intermetallic distance and angles, important bond length and angles, powder XRD diffraction profiles, TGA curves, plots of the experimental heat capacities of **1**−**4**, standard thermodynamic functions for **1**−**4**, and crystallographic data for **5** (PDF)

Crystallographic data for **1**−**5** (ZIP)

Accession Codes

CCDC 1858090, 1858093, 1858095, 2044510, and 2044511 for **1-5**, respectively, contain the supplementary crystallographic data for this paper. These data can be obtained free of charge *via* www.ccdc.cam.ac.uk/data_request/cif, or by emailing data_request@ccdc.cam.ac.uk, or by contacting The Cambridge Crystallographic Data Centre, 12 Union Road, Cambridge CB2 1EZ, UK; fax: +44 1223 336033.

■ AUTHOR INFORMATION

Corresponding Author

Ming-li Liu − *College of Chemistry and Chemical Engineering, Dezhou University, Dezhou 253023, P. R. China;* orcid.org/0000-0001-9980-4807; Phone: 86-0534-8987866; Email: liumingli0815@126.com

Authors

Quan Shi − *Thermochemistry Laboratory, Liaoning Province Key Laboratory of Thermochemistry for Energy and Materials, Dalian National Laboratory for Clean Energy, Dalian Institute of Chemical Physics, Chinese Academy of Sciences, Dalian 116023, P. R. China;* orcid.org/0000-0002-8792-0533

Lei-fang Liu − *College of Chemistry and Chemical Engineering, Dezhou University, Dezhou 253023, P. R. China*

Wen-bo Li − *College of Chemistry and Chemical Engineering, Dezhou University, Dezhou 253023, P. R. China*

Complete contact information is available at: https://pubs.acs.org/10.1021/acsomega.1c01052

Notes

The authors declare no competing financial interest.

■ ACKNOWLEDGMENTS

This work was supported by the NSFC of China (nos. 21501022 and 21601028), the Natural Science Foundation of Shandong Province (no. ZR2019QB026), and the Key Research and Development Program of Shandong Province (no. 2019GSF109039).

■ REFERENCES

(1) Liu, Q.; Yang, J.-M.; Guo, F.; Jin, L.-N.; Sun, W.-Y. Facile fabrication of MIL-103(Eu) porous coordination polymer nanostructures and their sorption and sensing properties. *Dalton Trans.* **2016**, *45*, 5841−5847.

(2) Cui, P.-P.; Zhang, X.-D.; Zhao, Y.; Fu, A.-Y.; Sun, W.-Y. Synthesis, structure and adsorption properties of lanthanide−organic frameworks with pyridine- 3,5-bis(phenyl-4-carboxylate). *Dalton Trans.* **2016**, *45*, 2591−2597.

(3) Luo, J.; Xu, H.; Liu, Y.; Zhao, Y.; Daemen, L. L.; Brown, C.; Timofeeva, T. V.; Ma, S.; Zhou, H.-C. Hydrogen Adsorption in a Highly Stable Porous Rare-Earth Metal-Organic Framework: Sorption Properties and Neutron Diffraction Studies. *J. Am. Chem. Soc.* **2008**, *130*, 9626−9627.

(4) Pan, L.; Adams, K. M.; Hernandez, H. E.; Wang, X.; Zheng, C.; Hattori, Y.; Kaneko, K. Porous Lanthanide-Organic Frameworks: Synthesis, Characterization, and Unprecedented Gas Adsorption Properties. *J. Am. Chem. Soc.* **2003**, *125*, 3062−3067.

(5) Kumar, M.; Li, L.-Q.; Zaręba, J. K.; Tashi, L.; Sahoo, S. C.; Nyk, M.; Liu, S.-J.; Sheikh, H. N. Lanthanide Contraction in Action: Structural Variations in 13 Lanthanide(III) Thiophene-2,5-dicarboxylate Coordination Polymers (Ln = La-Lu, Except Pm and Tm) Featuring Magnetocaloric Effect, Slow Magnetic Relaxation, and Luminescence-Lifetime-based Thermometry. *Cryst. Growth Des.* **2020**, *20*, 6430−6452.

(6) Zhang, X.; Vieru, V.; Feng, X.; Liu, J.-L.; Zhang, Z.; Na, B.; Shi, W.; Wang, B.-W.; Powell, A. K.; Chibotaru, L. F.; Gao, S.; Cheng, P.; Long, J. R. Influence of Guest Exchange on the Magnetization Dynamics of Dilanthanide Single-Molecule-Magnet Nodes within a Metal-Organic Framework. *Angew. Chem., Int. Ed.* **2015**, *54*, 9861−9865.

(7) Zhang, J.-W.; Kan, X.-M.; Liu, B.-Q.; Liu, G.-C.; Tian, A.-X.; Wang, X.-L. Systematic Investigation of Reaction-Time Dependence of Three Series of Copper-Lanthanide/Lanthanide Coordination Polymers: Syntheses, Structures, Photoluminescence, and Magnetism. *Chem.—Eur. J.* **2015**, *21*, 16219−16228.

(8) Bünzli, J.-C. G. Review: Lanthanide coordination chemistry: from old concepts to coordination polymers. *J. Coord. Chem.* **2014**, *67*, 3706−3733.

(9) Xiang, Z.; Fang, C.; Leng, S.; Cao, D. An amino group functionalized metal−organic framework as a luminescent probe for highly selective sensing of Fe^{3+} ions. *J. Mater. Chem. A* **2014**, *2*, 7662−7665.

(10) Sahoo, J.; Arunachalam, R.; Subramanian, P. S.; Suresh, E.; Valkonen, A.; Rissanen, K.; Albrecht, M. Coordinatively Unsaturated Lanthanide(III) Helicat -es: Luminescence Sensors for Adenosine Monophosphate in Aqueous Media. *Angew. Chem., Int. Ed.* **2016**, *55*, 1−6.

(11) Li, Z.; Li, P.; Xu, Q.; Li, H. Europium(iii)-β-diketonate complex-containing nanohybrid luminescent pH detector. *Chem. Commun.* **2015**, *51*, 10644−10647.

(12) Liu, D.; Lang, J.-P.; Abrahams, B. F. Highly Efficient Separation of a Solid Mixture of Naphthalene and Anthracene by a Reusable Porous Metal-Organic Framework through a Single-Crystal-to-Single-Crystal Transformation. *J. Am. Chem. Soc.* **2011**, *133*, 11042−11045.

(13) Wang, X.; Zhang, L.; Yang, J.; Liu, F.; Dai, F.; Wang, R.; Sun, D. Lanthanide metal-organic frameworks containing a novel flexible ligand for luminescence sensing of small organic molecules and selective adsorption. *J. Mater. Chem. A* **2015**, *3*, 12777−12785.

(14) Schäferling, M.; Ääritalo, T.; Soukka, T. Multidentate Europium Chelates as Luminoionophores for Anion Recognition: Impact of

Ligand Design on Sensitivity and Selectivity, and Applicability to Enzymatic Assays. *Chem.—Eur. J.* **2014**, *20*, 5298−5308.
(15) Seth, S.; Savitha, G.; Moorthy, J. N. Diverse isostructural MOFs by postsynthetic metal node metathesis: anionic-to-cationic framework conversion, luminescence and separation of dyes. *J. Mater. Chem. A* **2015**, *3*, 22915−22922.
(16) Qin, J.-S.; Zhang, S.-R.; Du, D.-Y.; Shen, P.; Bao, S.-J.; Lan, Y.-Q.; Su, Z.-M. A Microporous Anionic Metal-Organic Framework for Sensing Luminescence of Lanthanide(III) Ions and Selective Absorption of Dyes by Ionic Exchange. *Chem.—Eur. J.* **2014**, *20*, 5625−5630.
(17) Bünzli, J.-C. G. Lanthanide Luminescence for Biomedical Analyses and Imaging. *Chem. Rev.* **2010**, *110*, 2729−2755.
(18) Eliseeva, S. V.; Bünzli, J.-C. G. Lanthanide luminescence for functional materials and bio-sciences. *Chem. Soc. Rev.* **2010**, *39*, 189−227.
(19) Thibon, A.; Pierre, V. C. Principles of responsive lanthanide-based luminescent probes for cellular imaging. *Anal. Bioanal. Chem.* **2009**, *394*, 107−120.
(20) Parker, D. Critical Design Factors for Optical Imaging with Metal Coordination Complexes. *Aust. J. Chem.* **2011**, *64*, 239−243.
(21) Allain, C.; Faulkner, S. Photophysical approaches to responsive optical probes. *Future Med. Chem.* **2010**, *2*, 339−350.
(22) Song, X.-Q.; Meng, H.-H.; Lin, Z.-G.; Wang, L. 2D Lanthanide Coordination Polymers: Synthesis, Structure, Luminescent Properties, and Ratiometric Sensing Application in the Hydrostable PMMA-Doped Hybrid Films. *ACS Appl. Polym. Mater.* **2020**, *2*, 1644−1655.
(23) Ye, J.-W.; Lin, J.-M.; Mo, Z.-W.; He, C.-T.; Zhou, H.-L.; Zhang, J.-P.; Chen, X.-M. Mixed-Lanthanide Porous Coordination Polymers Showing Range-Tunable Ratiometric Luminescence for O2 Sensing. *Inorg. Chem.* **2017**, *56*, 4238−4243.
(24) Einkauf, J. D.; Clark, J. M.; Paulive, A.; Tanner, G. P.; de Lill, D. T. A General Model of Sensitized Luminescence in Lanthanide-Based Coordination Polymers and Metal-Organic Framework Materials. *Inorg. Chem.* **2017**, *56*, 5544−5552.
(25) Hagan, A. K.; Zuchner, T. Lanthanide-based time-resolved luminescence immunoassays. *Anal. Bioanal. Chem.* **2011**, *400*, 2847−2864.
(26) Moore, E. G.; Samuel, A. P. S.; Raymond, K. N. From Antenna to Assay: Lessons Learned in Lanthanide Luminescence. *Acc. Chem. Res.* **2009**, *42*, 542−552.
(27) Carr, R.; Evans, N. H.; Parker, D. Lanthanide complexes as chiral probes exploiting circularly polarized luminescence. *Chem. Soc. Rev.* **2012**, *41*, 7673−7686.
(28) Cable, M. L.; Levine, D. J.; Kirby, J. P.; Gray, H. B.; Ponce, A. Luminescent lanthanide sensors. *Adv. Inorg. Chem.* **2011**, *63*, 1.
(29) Bünzli, J.-C. G.; Eliseeva, S. V. Lanthanide NIR luminescence for telecommunications, bioanalyses and solar energy conversion. *J. Rare Earths* **2010**, *28*, 824−842.
(30) Ramya, A. R.; Sharma, D.; Natarajan, S.; Reddy, M. L. P. Highly Luminescent and Thermally Stable Lanthanide Coordination Polymers Designed from 4-(Dipyridin-2-yl)aminobenzoate: Efficient Energy Transfer from Tb3+ to Eu3+ in a Mixed Lanthanide Coordination Compound. *Inorg. Chem.* **2012**, *51*, 8818−8826.
(31) Carlos, L. D.; Ferreira, R. A. S.; de Zea Bermudez, V.; Julián-López, B.; Escribano, P. Progress on lanthanide-based organic-inorganic hybrid phosphors. *Chem. Soc. Rev.* **2011**, *40*, 536−549.
(32) Thejo Kalyani, N.; Dhoble, S. J. Organic light emitting diodes: Energy saving lighting technology-A review. *Renewable Sustainable Energy Rev.* **2012**, *16*, 2696−2723.
(33) Evans, R. C.; Douglas, P.; Winscom, C. J. Coordination complexes exhibiting room-temperature phosphorescence: Evaluation of their suitability as triplet emitters in organic light emitting diodes. *Coord. Chem. Rev.* **2006**, *250*, 2093−2126.
(34) Wang, J.; Suffren, Y.; Daiguebonne, C.; Freslon, S.; Bernot, K.; Calvez, G.; Le Pollès, L.; Roiland, C.; Guillou, O. Multi-Emissive Lanthanide-Based Coordination Polymers for Potential Application as Luminescent Bar-Codes. *Inorg. Chem.* **2019**, *58*, 2659−2668.
(35) Fu, R.; Hu, S.; Sheng, T.; Wu, X. Synthesis, crystal structures, and luminescent properties of eleven new lanthanide and yttrium complexes with fluorescent whitener and 1,10-phenanthroline. *New J. Chem.* **2009**, *33*, 1508−1514.
(36) Zheng, S.-R.; Chen, R.-L.; Liu, Z.-M.; Wen, X.-L.; Xie, T.; Fan, J.; Zhang, W.-G. Construction of terpyridine-Ln(iii) coordination polymers: structural diversity, visible and NIR luminescence properties and response to nerve-agent mimics. *CrystEngComm* **2014**, *16*, 2898−2909.
(37) Roberts, R. J.; Le, D.; Leznoff, D. B. Color-Tunable and White-Light Luminescence in Lanthanide-Dicyanoaurate Coordination Polymers. *Inorg. Chem.* **2017**, *56*, 7948−7959.
(38) Dannenbauer, N.; Matthes, P. R.; Scheller, T. P.; Nitsch, J.; Zottnick, S. H.; Gernert, M. S.; Steffen, A.; Lambert, C.; Müller-Buschbaum, K. Near-Infrared Luminescence and Inner Filter Effects of Lanthanide Coordination Polymers with 1,2-Di(4-pyridyl)ethylene. *Inorg. Chem.* **2016**, *55*, 7396−7406.
(39) Li, L.; Cheng, J.; Liu, Z.; Song, L.; You, Y.; Zhou, X.; Huang, W. Ratiometric Luminescent Sensor of Picric Acid Based on the Dual-Emission Mixed-Lanthanide Coordination Polymer. *ACS Appl. Mater. Interfaces* **2018**, *10*, 44109−44115.
(40) Abdallah, A.; Freslon, S.; Fan, X.; Rojo, A.; Daiguebonne, C.; Suffren, Y.; Bernot, K.; Calvez, G.; Roisnel, T.; Guillou, O. Lanthanide-Based Coordination Polymers With 1,4-Carboxyphenylboronic Ligand: Multiemissive Compounds for Multisensitive Luminescent Thermometric Probes. *Inorg. Chem.* **2019**, *58*, 462−475.
(41) Pointel, Y.; Suffren, Y.; Daiguebonne, C.; Le Natur, F.; Freslon, S.; Calvez, G.; Bernot, K.; Guillou, O. Rational Design of Dual IR and Visible Highly Luminescent Light-Lanthanides-Based Coordination Polymers. *Inorg. Chem.* **2020**, *59*, 10673−10687.
(42) Wu, C.-D.; Lu, C.-Z.; Lin, X.; Wu, D.-M.; Lu, S.-F.; Zhuang, H.-H.; Huang, J.-S. A novel left-handed double helicate constructed from L-tartrate bridged molybdenum(VI) and gadolinium(III) atoms. *Chem. Commun.* **2003**, 1284−1285.
(43) Wang, X.-L.; Qin, C.; Wang, E.-B.; Xu, L.; Su, Z.-M.; Hu, C.-W. Interlocked and Interdigitated Architectures from Self-Assembly of Long Flexible Ligands and Cadmium Salts. *Angew. Chem., Int. Ed.* **2004**, *43*, 5036−5040.
(44) Sailaja, S.; Rajasekharan, M. V. One-Dimensional Coordination Polymers of Silver(I) with Aminomethylpyridines. Example of a Triple Helical Infinite Chain. *Inorg. Chem.* **2000**, *39*, 4586−4590.
(45) Xing, K.; Fan, R.; Wang, F.; Nie, H.; Du, X.; Gai, S.; Wang, P.; Yang, Y. Dual-Stimulus-Triggered Programmable Drug Release and Luminescent Ratiometric pH Sensing from Chemically Stable Biocompatible Zinc Metal-Organic Framework. *ACS Appl. Mater. Interfaces* **2018**, *10*, 22746−22756.
(46) Banerjee, S.; Dastidar, P. Coordination Polymers in Selective Separation of Cations and Anions: A Series of Rarely Observed All Helical Three-Dimensional Coordination Polymers Derived from Various Chiral Amino Acid Based Bis-pyridyl-bis-amide Ligands. *Cryst. Growth Des.* **2011**, *11*, 5592−5597.
(47) Casini, A.; Woods, B.; Wenzel, M. The Promise of Self-Assembled 3D Supramolecular Coordination Complexes for Biomedical Applications. *Inorg. Chem.* **2017**, *56*, 14715−14729.
(48) Zhao, Z.; Zhang, Z.; Chen, L.; Cao, Y.; He, C.; Chen, X. Biodegradable Stereocomplex Micelles Based on Dextran-block-polylactide as Efficient Drug Deliveries. *Langmuir* **2013**, *29*, 13072−13080.
(49) Rojas, S.; Carmona, F. J.; Maldonado, C. R.; Horcajada, P.; Hidalgo, T.; Serre, C.; Navarro, J. A. R.; Barea, E. Nanoscaled Zinc Pyrazolate Metal-Organic Frameworks as Drug-Delivery Systems. *Inorg. Chem.* **2016**, *55*, 2650−2663.
(50) Karmakar, A.; Rúbio, G. M. D. M.; Guedes da Silva, M. F. C.; Hazra, S.; Pombeiro, A. J. L. Solvent-Dependent Structural Variation of Zinc(II) Coordination Polymers and Their Catalytic Activity in the Knoevenagel Condensation Reaction. *Cryst. Growth Des.* **2015**, *15*, 4185−4197.
(51) Yashima, E.; Ousaka, N.; Taura, D.; Shimomura, K.; Ikai, T.; Maeda, K. Supramolecular Helical Systems: Helical Assemblies of Small

https://doi.org/10.1021/acsomega.1c01052
ACS Omega 2021, 6, 10475−10485

Molecules, Foldamers, and Polymers with Chiral Amplification and Their Functions. *Chem. Rev.* **2016**, *116*, 13752−13990.
(52) Liebing, P.; Witzorke, J.; Oehler, F.; Schmeide, M. Dithiocarbamatocarboxylate (DTCC) Ligands-Building Blocks for Hard/Soft-Heterobimetallic Coordination Polymers. *Inorg. Chem.* **2020**, *59*, 2825−2832.
(53) Terzopoulou, A.; Nicholas, J. D.; Chen, X.-Z.; Nelson, B. J.; Pané, S.; Puigmartí-Luis, J. Metal-Organic Frameworks in Motion. *Chem. Rev.* **2020**, *120*, 11175−11193.
(54) Bespyatov, M. A. Low-Temperature Heat Capacity and Thermodynamic Functions of Tetrameric Cobalt(II) Acetylacetonate. *J. Chem. Eng. Data* **2020**, *65*, 5218−5225.
(55) Smith, A. L.; Colineau, E.; Griveau, J.-C.; Popa, K.; Kauric, G.; Martin, P.; Scheinost, A. C.; Cheetham, A. K.; Konings, R. J. M. A New Look at the Structural and Magnetic Properties of Potassium Neptunate K_2NpO_4 Combining XRD, XANES Spectroscopy, and Low-Temperature Heat Capacity. *Inorg. Chem.* **2017**, *56*, 5839−5850.
(56) Wei, L.; Xinmin, W.; Zhicheng, T.; Songsheng, Q. Low-Temperature Heat Capacity and Enthalpy of Formation of $[Er_2(Gly)_6(H_2O)_4](ClO_4)_6{\cdot}5H_2O$. *J. Chem. Eng. Data* **2007**, *52*, 1182−1185.
(57) Rosen, P. F.; Dickson, M. S.; Calvin, J. J.; Ross, N. L.; Friščić, T.; Navrotsky, A.; Woodfield, B. F. Thermodynamic Evidence of Structural Transformations in CO2-Loaded Metal−Organic Framework Zn-$(MeIm)_2$ from Heat Capacity Measurements. *J. Am. Chem. Soc.* **2020**, *142*, 4833−4841.
(58) Zou, G.; Cheng, Z.; Zhang, S.; Tan, Z.; Zhang, J.; Shi, Q. Calorimetric studies on two halogenated uracil isomers. *Thermochim. Acta* **2016**, *634*, 6−11.
(59) Zhang, H.; Yang, L.-M.; Ganz, E. Adsorption Properties and Microscopic Mechanism of CO2 Capture in 1,1-Dimethyl-1,2-ethylenediamine-Grafted Metal-Organic Frameworks. *ACS Appl. Mater. Interfaces* **2020**, *12*, 18533−18540.
(60) Zhang, H.; Yang, L.-M.; Ganz, E. Unveiling the Molecular Mechanism of CO2 Capture in N-Methylethylenediamine-Grafted M2(dobpdc). *ACS Sustainable Chem. Eng.* **2020**, *8*, 14616−14626.
(61) Zhang, H.; Yang, L.-M.; Pan, H.; Ganz, E. Atomistic Level Mechanism of CO2 Adsorption in N-Ethylethylenediamine-Functionalized M2(dobpdc) Metal-Organic Frameworks. *Cryst. Growth Des.* **2020**, *20*, 6337−6345.
(62) Zhang, H.; Shang, C.; Yang, L.-M.; Ganz, E. Elucidation of the Underlying Mechanism of CO2 Capture by Ethylenediamine-Functionalized M2(dobpdc) (M = Mg, Sc-Zn). *Inorg. Chem.* **2020**, *59*, 16665−16671.
(63) Zhang, H.; Yang, L.-M.; Ganz, E. Formation Mechanism of Ammonium Carbamate for CO2 Uptake in N,N′-Dimethylethylenediamine Grafted M2(dobpdc). *Langmuir* **2020**, *36*, 14104−14112.
(64) Zhang, H.; Yang, L.-M.; Pan, H.; Ganz, E. Disclosing the microscopic mechanism and adsorption properties of CO2 capture in *N*-isopropylethylenediamine appended M2(dobpdc) series. *Phys. Chem. Chem. Phys.* **2020**, *22*, 24614−24623.
(65) Liu, Y.; Pan, M.; Yang, Q.-Y.; Fu, L.; Li, K.; Wei, S.-C.; Su, C.-Y. Dual-emission from a single-phase Eu-Ag metal-organic framework: an alternative way to get white-light phosphor. *Chem. Mater.* **2012**, *24*, 1954−1960.
(66) Manzur, J.; de Santana, R. C.; Maia, L. J. Q.; Vega, A.; Spodine, E. Tuning White Light Emission in Dinuclear Phenoxo Bridged DyIII Complexes. *Inorg. Chem.* **2019**, *58*, 10012−10018.
(67) Hu, L.-X.; Gao, M.; Wen, T.; Kang, Y.; Chen, S. Synthesis of Halide-Modulated Cuprous(I) Coordination Polymers with Mechanochromic and Photocatalytic Properties. *Inorg. Chem.* **2017**, *56*, 6507−6511.
(68) Sun, Y.-g.; Gu, X.-f.; Ding, F.; Smet, P. F.; Gao, E.-j.; Poelman, D.; Verpoort, F. Synthesis, Crystal Structures, and Properties of Novel Heterometallic La/Pr−Cu−K and Sm/Eu/Tb−Cu Coordination Polymers. *Cryst. Growth Des.* **2010**, *10*, 1059−1067.
(69) Freslon, S.; Luo, Y.; Daiguebonne, C.; Calvez, G.; Bernot, K.; Guillou, O. Brightness and Color Tuning in a Series of Lanthanide-Based Coordination Polymers with Benzene-1,2,4,5-tetracarboxylic Acid as a Ligand. *Inorg. Chem.* **2016**, *55*, 794−802.
(70) Liu, M.-L.; Shi, W.; Song, H.-B.; Cheng, P.; Liao, D.-Z.; Yan, S.-P. Open and closed copper chain coordination polymers with alternating ferromagnetic and antiferromagnetic interactions. *CrystEngComm* **2009**, *11*, 102−108.
(71) Lymperopoulou, S.; Lazarides, T.; Papachristodoulou, C.; Raptopoulou, C. P.; Psycharis, V.; Plakatouras, J. C. Synthesis, structural characterization, and fluorescence of a series of 1D rare earth coordination polymers with a substituted iminodiacetate ligand. *Inorg. Chim. Acta* **2018**, *472*, 276−282.
(72) Kumar, M.; Kariem, M.; Sheikh, H. N.; Frontera, A.; Seth, S. K.; Jassal, A. K. A series of 3D lanthanide coordination polymers decorated with a rigid 3,5-pyridinedicarboxylic acid linker: syntheses, structural diversity, DFT study, Hirshfeld surface analysis, luminescence and magnetic properties. *Dalton Trans.* **2018**, *47*, 12318−12336.
(73) Vicentini, G.; Zinner, L. B.; Zukerman-Schpector, J.; Zinner, K. Luminescence and structure of europium compounds. *Coord. Chem. Rev.* **2000**, *196*, 353−382.
(74) Arnaud, N.; Vaquer, E.; Georges, J. Comparative study of the luminescent properties of europium and terbium coordinated with thenoyltrifluoroacetone or pyridine-2,6-dicarboxylic acid in aqueous solutions. *Analyst* **1998**, *123*, 261−265.
(75) Zhang, X.; Zhan, Z.; Liang, X.; Chen, C.; Liu, X.; Jia, Y.; Hu, M. Lanthanide-MOFs constructed from mixed dicarboxylate ligands as selective multi-responsive luminescent sensors. *Dalton Trans.* **2018**, *47*, 3272−3282.
(76) Feng, X.; Liu, B.; Wang, L.-Y.; Zhao, J.-S.; Wang, J. G.; Weng, N. S.; Shi, X.-G. A series of lanthanide-organic polymers incorporating nitrogen-heterocyclic and aliphatic carboxylate mixed-ligands: structures, luminescent and magnetic properties. *Dalton Trans.* **2010**, *39*, 8038−8049.
(77) Sethi, W.; Sanz, S.; Pedersen, K. S.; Sørensen, M. A.; Nichol, G. S.; Lorusso, G.; Evangelisti, M.; Brechin, E. K.; Piligkos, S. Magnetic and magnetocaloric properties of an unusual family of carbonate-panelled $[Ln^{III}_6Zn^{II}_2]$ cages. *Dalton Trans.* **2015**, *44*, 10315−10320.
(78) Tan, X.-F.; Zhou, J.; Zou, H.-H.; Fu, L.; Tang, Q.; Wang, P. A series of lanthanide glutarates: lanthanide contraction effect on crystal frameworks of lanthanide glutarates. *RSC Adv.* **2017**, *7*, 17934−17940.
(79) Zheng, Y.-Z.; Zheng, Z.; Chen, X.-M. A symbol approach for classification of molecule-based magnetic materials exemplified by coordination polymers of metal carboxylates. *Coord. Chem. Rev.* **2014**, *258*−*259*, 1−15.
(80) Benmerad, B.; Aliouane, K.; Rahahlia, N.; Guehria-Laïdoudi, A.; Dahaoui, S.; Lecomte, C. Studies of two lanthanide coordination polymers built up from dinuclear units. *J. Rare Earths* **2013**, *31*, 85−93.
(81) Gopal, E. S. R. *Specific Heat at Low Temperatures (International Cryogenics Monogra ph Series)*; Plenum Press: New York, 1966.
(82) Snow, C. L.; Lilova, K. I.; Radha, A. V.; Shi, Q.; Smith, S.; Navrotsky, A.; Boerio-Goates, J.; Woodfield, B. F. Heat capacity and thermodynamics of a synthetic two-line ferrihydrite, $FeOOH{\cdot}0.027H_2O$. *J. Chem. Thermodyn.* **2013**, *58*, 307−314.
(83) Woodfield, B. F.; Shapiro, J. L.; Stevens, R.; Boerio-Goates, J.; Putnam, R. L.; Helean, K. B.; Navrotsky, A. Molar heat capacity and thermodynamic functions for $CaTiO_3$. *J. Chem. Thermodyn.* **1999**, *31*, 1573−1583.
(84) Yang, Q.; Ge, J.; Liu, X.; Shi, Q.; Ke, H.; Wei, Q.; Xie, G.; Chen, S.; Gao, S. Low temperature heat capacity, standard entropy, standard enthalpy and magnetic property: a new 1D CuII coordination polymer incorporating tetrazole-1-acetic acid and *p*-nitrobenzoic acid. *Dalton Trans.* **2017**, *46*, 1878−1884.
(85) Xu, Y.; Yuan, D.; Wu, B.; Han, L.; Wu, M.; Jiang, F.; Hong, M. 1D Tube, 2D Layer, and 3D Framework Derived from a New Series of Metal(II)−5-Aminodiacetic Isophthalate Coordination Polymers. *Cryst. Growth Des.* **2006**, *6*, 1168−1174.
(86) Lymperopoulou, S.; Papastergiou, M.; Louloudi, M.; Raptopoulou, C. P.; Psycharis, V.; Milios, C. J.; Plakatouras, J. C. Synthesis, Characterization, Magnetic and Catalytic Properties of a

https://doi.org/10.1021/acsomega.1c01052
ACS Omega 2021, 6, 10475−10485

Ladder-Shaped Mn^{II} Coordination Polymer. *Eur. J. Inorg. Chem.* **2014**, *2014*, 3638−3644.
(87) Sheldrick, G. M. A short history ofSHELX. *Acta Crystallogr.* **2008**, *64*, 112−122.
(88) Sheldrick, G. M. *SHELXS-97, Program for X-ray Crystal Structure Determination*; University of Göttingen: Germany, 1997.
(89) Sheldrick, G. M. Crystal structure refinement withSHELXL. *Acta Crystallogr.* **2015**, *71*, 3−8.

https://doi.org/10.1021/acsomega.1c01052
ACS Omega 2021, 6, 10475−10485